Photothermal self-healing of gold nanoparticle-polystyrene hybrids

Journal:	*Nanoscale*
Manuscript ID	NR-ART-07-2020-005621.R1
Article Type:	Paper
Date Submitted by the Author:	24-Sep-2020
Complete List of Authors:	Cho, Yi Je; Virginia Polytechnic Institute and State University, Department of Materials Science and Engineering Kong, Lingchen; Virginia Polytechnic Institute and State University, Department of Materials Science and Engineering Islam, Rezawana; Virginia Polytechnic Institute and State University, Department of Materials Science and Engineering Nie, Meitong; Virginia Polytechnic Institute and State University, Department of Electrical and Computer Engineering Zhou, Wei; Virginia Polytechnic Institute and State University, Department of Electrical and Computer Engineering Lu, Kathy; Virginia Polytechnic Institute and State University, Department of Materials Science and Engineering

ARTICLE

Photothermal self-healing of gold nanoparticle-polystyrene hybrids

Received 00th January 20xx,
Accepted 00th January 20xx

DOI: 10.1039/x0xx00000x

Yi Je Cho[a], Lingchen Kong[a], Rezawana Islam[a], Meitong Nie[b], Wei Zhou[b], and Kathy Lu*[a]

This study focused on the processing and photothermal healing of gold nanoparticle (Au NP) and polystyrene (PS) hybrid films. Effects of Au NP contents were investigated using hybrid films with the NP content from 0 to 1 wt% via a solvent-assisted approach. The as-synthesized Au NPs showed an average diameter of 4-5 nm with a face-centered cubic structure. The Au NP agglomeration deteriorated as the content increased and the interparticle distance decreased. The film transparency and flexibility also decreased with the NP content. The Au-PS films demonstrated desirable photothermal healing behaviors, which required more energy with the defect size increase. The simulated temperature distribution on the hybrid films during the photo-induced healing showed good agreement with the experimental results, with particle agglomeration degrading the healing properties. The developed hybrid films can be used in functional devices and coatings with high flexibility and healed using photon energy sources.

Introduction

Functional nanoparticles and a flexible polymer matrix, when integrated at the single nanometer level, are an exciting class of hybrid materials. Their properties can be tailored to combine the desirable characteristics of multiple species, realize new functionality, and create new features. Nanoparticle (NP)-polymer hybrid materials, especially when processed into thin films, are one class of hybrid materials that can yield various novel properties such as electrical, optical, mechanical, thermal, dielectric, and magnetic behaviors.[1-4] Also, any processing methods used to produce polymers can be adopted for the hybrid materials with small modifications.[5, 6] This advantage also implies low production cost of the polymer hybrids. Their potential applications range widely from energy conversion to memory storage and to foldable screens.[7]

With the continuous understanding and advancement of NP-polymer hybrids, two important aspects need to be addressed. One is flexibility and the other is defect repair (healing) ability of the hybrid films. Repeated bending and shape distortion of the films during lifetime can result in premature failures and shortened component life. To create highly flexible hybrid films, nanoparticles must decrease to a certain size and their distributions in the hybrid film need to be uniform. Appropriate flexibility assessment is also needed in order to compare the characteristics of different hybrid films and accurately predict their behaviours in device uses. Currently, the flexibility of polymer nanocomposites is either measured by manually bending a film[8] or by testing its bending radius.[9, 10] There is a lack of study of the effect of cyclic bending. In flexible electronics, bending fatigue assessment is needed for reliability and property change understanding.[11-14]

When hybrid films are damaged by external distortion forces,[15-17] healing ability for the damaged films is much needed in order to maintain the performance and extend the lifetime of the corresponding devices.[17-19] Intrinsic self-healing polymers can be obtained through reversible molecular interactions from the polymer matrix.[17, 18] However, the majority of their self-healing reactions occur at high temperatures, or the networks themselves exhibit undesirably low glass transition temperatures.[20] To meet the requirements of many device use conditions, extrinsic healing polymers have been more attractive.[20] Several healing agents have been utilized: encapsulation of reactive agents and crosslinking reactants,[21] 3D microvascular networks filled with reactive crosslinkers,[22] shape memory assisted self-healing polymers[23], and nanoparticles (NPs) with superparamagnetic or photothermal properties.[15, 24-27]

Inorganic particles with the photothermal effect can be a source for defect/damage healing. Among them, NPs such as gold and silver can heal polymers with selective wavelengths by converting electromagnetic radiation to heat.[20, 28] With the illumination of an incident electromagnetic beam, a localized surface plasmon resonance (LSPR) effect takes place; confinement and collective oscillation of these polarizable electrons lead to absorption of visible light.[29-32] The particle temperature can rise up to 700 °C, which in turn heats the surroundings.[33-37] The polymer matrix of the hybrids then flows when the temperature rises above the glass transition temperature. The damaged spots in the hybrid films can be filled back with flowing polymers without requirement of external contact with the films or any other structural/functional alternation. For example, when the glass

---

[a] Department of Materials Science and Engineering, Virginia Polytechnic Institute and State University, Blacksburg, Virginia 24061
[b] Department of Electrical and Computer Engineering, Virginia Polytechnic Institute and State University, Blacksburg, Virginia 24061

transition temperature of a polymer is ~495 °C, its healing can be sufficiently accomplished by the photothermal effect of Au NPs.[38] Additionally, Au NPs with sizes larger than 2 nm can reach 100% of light-to-heat conversion efficiency.[28] Such small, hybridized Au NPs in the films can also improve other functional properties such as power conversion efficiency in solar cells.[39]

The photothermal heating depends on the NP absorption efficiency and the incident light. The efficiency changes with NP size, shape, agglomeration state, and composition. The healing parameters related to the incident light are intensity, wavelength, pulse duration, and polarization.[40-42] The most straightforward approach to increase the efficiency in reaching a maximum temperature is by increasing the NP density (i.e. the number of NPs in the region of interest).[43] In addition, plasmons on distinct NPs can reciprocally influence each other, depending on interparticle distance, with the generation of hybrid plasmon modes, which is known as plasmonic coupling. This hybridization takes place if the interparticle distance is roughly less than 2.5 times of the diameter of two adjacent NPs, by enhancing the electric fields between neighbouring particles.[44-46] Therefore, NP density and distribution play an important role in the plasmonic coupling and thermal healing of NP-polymer films. Although numerous studies have been conducted on the effects of particle distance and distribution on the SPR change,[43-45, 47-50] the effects on the photothermal heating are rather less investigated. Among the few reported studies, 0.01–0.04 wt% 5 nm Au NPs were added to various polymers;[25] more NPs increased the maximum temperature, up to 250 °C. Also, a maximum temperature of 85 °C was achieved when 0.11 and 0.42 wt% 14 nm Au NPs were used in a polyethylene/poly(ethylene-*co*-vinyl acetate) blend film.[15] Even though both of these studies were able to achieve healing of the considered polymers, the effects of interparticle distance and distribution were not noted.

Numerical modelling can shed light on the theoretical photothermal behaviours of NPs with LSPR behaviours, which can account for many aspects of the phenomenon that cannot be experimentally obtained. So far, there have been some investigations on the temperature change and heat transfer at 1-2 particle level with consideration of the plasmonic coupling.[51-56] Even though multiple particles were involved, the distribution of the NPs was assumed uniform.[57-59] However, when Au NPs are embedded in a hybrid film, the spatial distribution is random, which strongly affects the SPR efficiency.[57, 58] Development of a numerical model and an investigation in the roles of Au NPs in a polymer matrix during photothermal processes are much needed for an improved understanding of microstructural parameters such as particle concentration and distribution.

This study is centred around the photo-induced healing efficiency of the Au NP-PS systems with Au NP concentrations up to 1 wt%. The characteristics of Au NPs, the flexibility of the Au-PS hybrid films, and the photo-induced healing behaviours of the films are examined. Furthermore, the effects of the Au NP concentration, agglomeration, and interparticle distance on the photothermal heating are analysed using two different scale finite element models.

Experimental

Material preparation

An aqueous solution of hydrogen tetrachloroaurate (99.9%, Fisher Scientific, USA) (30 mmol/L) was mixed with a solution of tetraoctylammonium bromide (98%, Fisher Scientific, USA) in toluene (50 mmol/L) with a ratio of 3:8. The two-phase mixture was vigorously stirred until all the tetrachloroaurate was transferred into the organic layer and dodecanethiol (55 wt% of $HAuCl_4$, 98%, Acros Organics, USA) was then added to the organic phase. A freshly prepared aqueous solution of sodium borohydride (5:6 with $HAuCl_4$ aqueous solution of 0.4 mol/L concentration) (96%, Sigma-Aldrich, USA) was slowly added with stirring. After further stirring for 3 h, the organic phase was separated, evaporated to the volume of 1:3 with the $HAuCl_4$ solution, and mixed with 40 times volume of ethanol to remove the excess dodecanethiol. The mixture was kept for 4 h at 0 ℃ and the dark brown precipitate was filtered off and washed with ethanol. The crude product was dissolved in toluene with a volume of 1:3 with the $HAuCl_4$ solution.

PS (molar weight at ~192,000, Sigma-Aldrich, USA) was fully dissolved in toluene at 10 wt% concentration by magnetic stirring for 12 h. The prepared Au solutions at different concentrations were mixed with the dissolved PS (at 0, 0.2, 0.4, 0.6, 0.8, and 1 wt% Au concentration) for 12 h to obtain the final hybrid suspensions. Drops of a specific Au-PS suspension were placed on a glass slide, which was functionalized with 1H,1H,2H,2H-perfluorodecyltrichlorosilane (97%, Sigma-Aldrich, USA) in an oven at 90 ℃ for 3 h and then at 130 ℃ for 3 h.[60] A doctor blade was used to cast the suspension drops on the glass slide to form a liquid film. The liquid film was put into a freeze dryer to remove any pores and then dried in a fume hood overnight. Finally, solid films with a thickness of ~50 μm were obtained. All the samples were maintained at the same thickness for consistency.

Material characterization

The size distribution of the Au NPs in suspension was measured using the dynamic light scattering (DLS) technique (Zetasizer Nano ZS, Malvern Panalytical, United Kingdom) at a fixed light scattering angle of 173°. This size was again confirmed under a transmission electron microscope (TEM; JEOL 2100, JEOL, Japan) at an accelerating voltage of 200 kV. A phase analysis was performed on the synthesized Au NPs using X-ray diffractometer (XRD; Panalytical B.V., Almelo, Netherlands) with Cu (Kα) radiation at 45 kV and 40 mA and a scan rate of 0.03°/s. The surface morphology of the hybrid film was characterized using scanning electron microscopy (SEM; Quanta 600 FEG, FEI Inc., Hillsboro, OR). The transparency of the films with different Au NP concentrations were compared using samples with a uniform size of 1.5 cm × 2 cm × 50 μm and confirmed through ultraviolet-visible spectroscopy (UV-Vis; HR2000CG-UV-NIR, Ocean Optics, USA), where the pure PS film was used as a reference.

For the flexibility testing, a lab-made device was used as shown in Fig. 1. It adopted the free arc bending test method

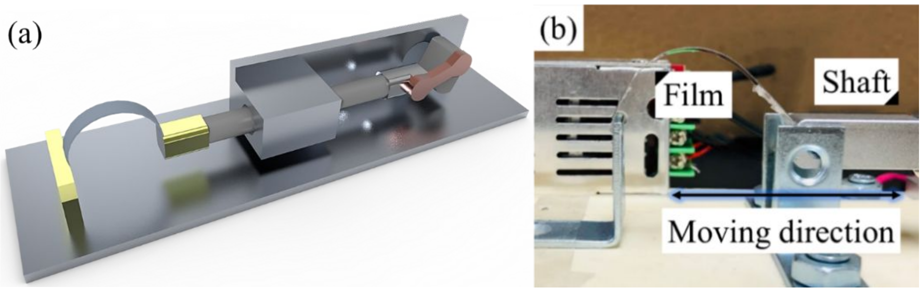

Fig. 1. (a) A schematic diagram of the flexibility testing device and (b) actual photograph of the device used in this study.

reported elsewhere.[14] The device consisted of a stepping motor (TS-37GB330, Tsiny Motor Industrial Co. Ltd, China) and a fixed stage, with the motor shaft surface and the stage surface on the same horizontal level. The hybrid film was securely fixed on the shaft surface of the stepping motor and the fixed stage surface using adhesive tapes to minimize stress concentration near the clamps. One end of the flexible film/specimen was fixed to the clamp and the other end (shaft) was allowed to move linearly at a speed of 23.5 mm/s. Through the motion control of the motor, the bending radius of the hybrid film was varied at different values. This arrangement provided repetitive compression by inner bending followed by tension during straightening. The bending cycles for each hybrid film were counted using a step counter (C1301-01, Inpelanyu, China). The thickness of the films was about 100 μm with a width of 7 mm. The bending radii were 6, 4, and 2 mm with a film length at 32, 30, and 28 mm, respectively. To determine the bending radius for the films with different lengths, tests were first conducted by bending the films with the highest concentration of Au NPs (1 wt%), as they were the most brittle samples. During the flexibility testing, the films were bent until they were cracked, then the bending radius before cracking was selected for the bending tests. The position of the clamp was adjusted to change the bending radii for the films with different lengths, while the rest of the components were fixed.

Before the photo-induced healing tests, a series of diamond-shaped indents with diagonal lengths of 30, 55, and 80 μm was created on the film with 100 μm thickness using a Vickers hardness indenter (900-390A, Phase II, USA) by applying 0.098, 0.245, and 0.490 N loads, respectively. The depth of the indents introduced to the films at the same load was almost identical regardless of the Au NP concentration. For instance, the depth was 15.4 and 15.1 μm for the films with 0.2 and 1.0 wt% Au NPs, respectively. For the healing tests, a frequency doubled Nd: YAG laser with 532 nm wavelength and 50 mW power at the laser output was used, which was a part of a Raman system (Alpha 300 RSA+, WItech, Germany) with an optical microscope for imaging. This system was equipped with a 20x objective lens with 0.4 NA, of which the ideal focused beam diameter was calculated as 665 nm based on the Abbe diffraction limit. However, at this focused position, the power density of the laser was too high and the films were burnt. Therefore, the sample stage was moved 90 μm away from the focused position to reduce the laser power by defocusing. As a result, the spot size of the beam was determined to be 100 μm, which was 8 μm larger than a theoretical beam diameter calculated based on the Gaussian beam properties. Also, the lowest laser power to heal the indents was checked by trial and error. The power of the laser irradiated to the indents was 12.25, 6.10, 3.86, 4.90, and 4.25 mW for the hybrid films with 0.2, 0.4, 0.6, 0.8, and 1.0 wt% Au NPs, respectively. During the healing process, the energy needed to heal the indents was calculated by the laser intensity, indent size, and irradiation time as $energy\,(J) = intensity * indent\ area * time$. The film temperature during irradiation was measured using an infrared camera (AX5, FLIR Systems, USA). Due to the relatively low resolution of the camera, the diameter of the laser spot was enlarged to a few millimeters so that the camera could recognize the heated area. As the laser intensity decreased with increasing laser spot size, the temperatures at the high intensities used in the healing tests were extrapolated using linear fitting by assuming the evolved temperature and the laser intensity had a linear relationship.

Simulation method

Finite element simulations of the electromagnetic response and heat transfer of the Au NP/PS hybrid films were performed using COMSOL Multiphysics. Two different scales were considered: 1) a nanoscale model to analyze the electromagnetic response, 2) a macroscale model to estimate the temperature distribution in the hybrid film.

Electromagnetic response and heat transfer

When the incident laser is irradiated on Au NPs, which are in proximity to each other, the scattering field on one particle can interact with that on the other particle. Therefore, the electric field strength $\mathbf{E}$ should be the sum of the incident electric field $\mathbf{E}_{inc}$ and the scattering field $\mathbf{E}_{sca}$ of the neighbouring particles:[61]

$$\mathbf{E} = \mathbf{E}_{inc} + \mathbf{E}_{sca} \quad (1)$$

When the incident laser travels along the positive x-direction and polarized along the z-direction, the incident electric field is expressed as,

$$\mathbf{E}_{inc} = \vec{x}E_0 e^{-j \cdot k_w \cdot z \cdot n_{PS}} \quad (2)$$

where E_0, e, k_w, and n_{PS} are the incident electric field, electron charge, wave number, and refractive index of PS, respectively.

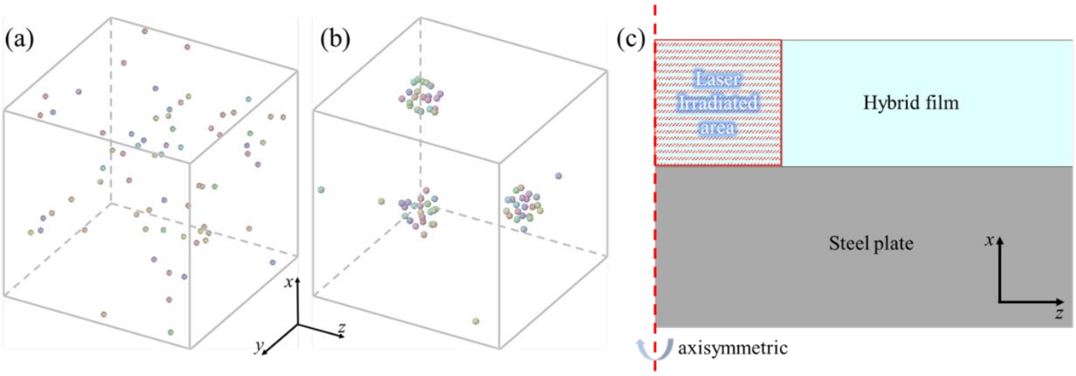

Fig. 2. Nanoscale models with 1 wt% Au NPs (a) in a random distribution and (b) in an agglomerated distribution with δ=0.90. (c) A macroscale model with a hybrid film and a steel plate.

In a region with a constant permittivity and no charge, the near-field can be calculated using Maxwell's equation as Helmholtz equation:[62, 63]

$$\nabla \times \nabla \times \mathbf{E}_{sca} - \omega^2 \varepsilon_0 \mu_0 \varepsilon_r \mathbf{E}_{sca} = 0 \tag{3}$$

where ω, ε_0, and μ_0 are the angular frequency, vacuum permittivity, and magnetic permeability in vacuum, respectively. The solution to the Helmholtz equation provides the electromagnetic behaviours of the Au NPs including electric field enhancement and absorption cross-section σ_{abs}.

The temperature distribution in the hybrid films owing to the photothermal effect is modelled by solving heat transfer equations. The individual NPs are regarded as heat sources. The temperature changes in the film are dependent on the energy of the Au NPs that is absorbed and dissipated during the laser emission. The heat source (absorbed power) by the Au NPs is given as,[54, 56, 58]

$$Q = \frac{\sigma_{abs} I}{V_{Au}} \tag{4}$$

where I and V_{Au} are intensity of the incident field and volume of one nanoparticle, respectively. The heat dissipated from the Au NPs generates the local temperature field in the PS matrix as a function of time, which is governed by the heat equation as,

$$\rho_{PS} C_{PS} \frac{\partial T_{PS}}{\partial t} = \nabla(\kappa_{PS} \nabla T_{PS}) + Q \tag{5}$$

where ρ_{PS}, C_{PS}, T_{PS} and κ_{PS} are the density, heat capacity, temperature, and thermal conductivity of PS, respectively.

Model

Two different types of the nanoscale model, one with a random distribution and the other with an agglomerated distribution of the Au NPs, were generated in order to consider the particle distribution effects. The agglomeration in this study means a non-uniform spatial distribution of the Au NPs and

Table 1. List of symbols used and their values with a brief description.

Symbol	Value (unit)	Description
λ	532 (nm)	wavelength of laser
E_0	sqrt($2I/c_0\varepsilon_0$) (V/m)	incident electric field
I	P/A (W/m^2)	intensity of incident field
P	varies with Au concentration (W)	power of incident field
A	100 (μm)	area of laser spot
ω	$2\pi c_0/\lambda$	angular frequency
ε_0	8.542187817 × 10^{-12} (F/m)	vacuum permittivity
μ_0	$4\pi \times 10^7$ (N/A^2)	magnetic permeability in vacuum
n_{Au}	0.54386	refractive index of Au at 532 nm (real)
k_{Au}	2.2309	refractive index of Au at 532 nm (imaginary)
ρ_{Au}	19.32 (g/cm^3)	density of Au
C_{Au}	129 (J/Kg·K)	heat capacity of Au
κ_{Au}	314 (W/m^2·K)	thermal conductivity of Au
n_{PS}	1.5983	refractive index of PS at 532 nm (real)
ρ_{PS}	1.05 (g/cm^3)	density of PS
C_{PS}	temperature dependent	heat capacity of PS
κ_{PS}	0.16 (W/m^2·K)	thermal conductivity of PS
ρ_{PS}	7.85 (g/cm^3)	density of steel
C_{PS}	475 (J/Kg·K)	heat capacity of steel
κ_{PS}	44.5 (W/m^2·K)	thermal conductivity of steel

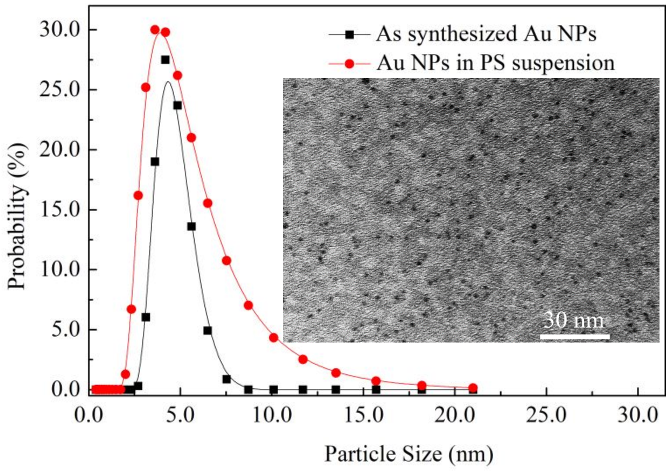

Fig. 3. Volume-averaged size distributions of the Au NPs before and after co-suspension with the PS polymer with a corresponding TEM image.

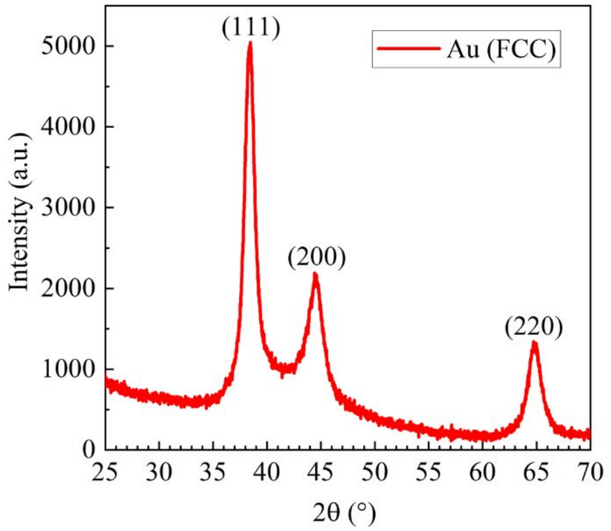

Fig. 4. XRD pattern of the synthesized Au nanoparticles.

represents the agglomeration of Au NPs. For the random distribution, the spherical Au NPs having a diameter of 5 nm were distributed in a three-dimensional cube with an edge length of 200 nm using the random sequential adsorption algorithm.[64] In this algorithm, when a newly added particle spatially overlapped with previously generated ones, it was deleted and then another particle was generated at a different location. This procedure continued until the volume percent of the NPs reached 0.011, 0.022, 0.033, 0.044, and 0.055%, which corresponded to the weight percent of 0.2, 0.4, 0.6, 0.8, and 1.0%, respectively, used in the experiments. In total, five models with randomly distributed NPs were constructed. The particles were avoided at the cube boundaries for simplicity. The typical geometry of the nanoscale models with a random Au NP distribution is shown in Fig. 2(a).

For the agglomerated Au NP distribution, the particle content was fixed as 1 wt%. First, three subdomains were generated in a cubic space, of which the local particle volume fraction was higher than the outside regions of the subdomains. The outside un-agglomerated region had a lower particle volume fraction than the average. An agglomeration parameter δ was introduced to characterize the agglomeration degree as $\delta = V_c/V_t$, where V_c and V_t were the particle volume fraction in the agglomerated region and total volume, respectively. δ=0.15, 0.30, 0.45, 0.60, 0.75, 0.90 were considered. The minimum distance between the particles was set as 1 nm. A typical 3D snapshot of the Au agglomeration model with δ=0.90 is shown in Fig. 2(b).

For the heat transfer analysis, a two-dimensional axisymmetric macroscale model consisting of a hybrid film with a thickness of 100 μm and a steel plate (the same configuration as in the experiments since the films were placed on the steel plate during the tests) was generated, which is shown in Fig. 2(c). The hybrid film was sectioned into two parts based on the diameter of the laser spot on the film; the part near the symmetric axis was an area where the laser was irradiated. The steel plate was included in the model because there might be heat transfer from the films to the plate causing the temperature change, however, even the different materials for the plate did not affect the temperature distribution.

The nanoscale models involved a controlled cubic volume called perfectly matched layer, with a size 20 times larger than the diameter of the NPs, which was adopted to prevent the light reflection. The incident electric field with a wavelength of 532 nm was linearly polarized along the z-axis with the propagation parallel to the positive x-axis. The absorption cross-section obtained after the electromagnetic analysis of the nanoscale model was used to calculate the heat source (absorbed power by the Au NPs) by Eq. (4). The heat transfer analysis involved two steps. First, the heat source from Eq. (4) at each NP was used to evaluate the volume-averaged heat source of the whole nanoscale model. Then, this volume-averaged value was used as the input to the macroscale model to investigate the temperature distribution at the steady-state condition. The constants and material properties are shown in Table 1. Although the hybrid film in the macroscale heat analysis was composed of the Au NPs and PS, the volume fraction of the Au NPs was significantly small enough to neglect the effects on the other properties of the hybrids. Therefore, the properties of PS were used for the hybrid film.

Result and discussion

Hybrid film characteristics

The volume-averaged size distributions of the Au NPs measured by the dynamic light scattering are shown in Fig. 3. The average size of the as-synthesized Au NPs is 4.3 nm. After co-dispersing with PS, the size increases slightly to 4.9 nm. The polydispersity index was 0.15 and 0.38 for the as-synthesized Au NPs and Au NPs in the PS suspension, respectively. The small difference is due to the disturbance of the dissolved PS polymer

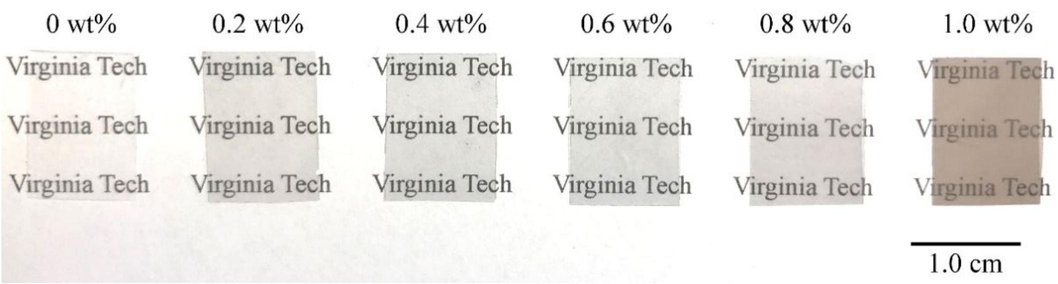

Fig. 5. Transparency of the Au-PS hybrid films with the Au NP concentration from 0 to 1 wt%.

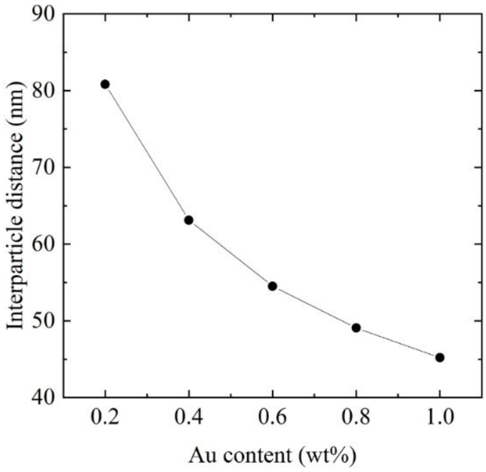

Fig. 6. Calculated Au interparticle spacing in the Au-PS hybrid films at different NP concentrations.

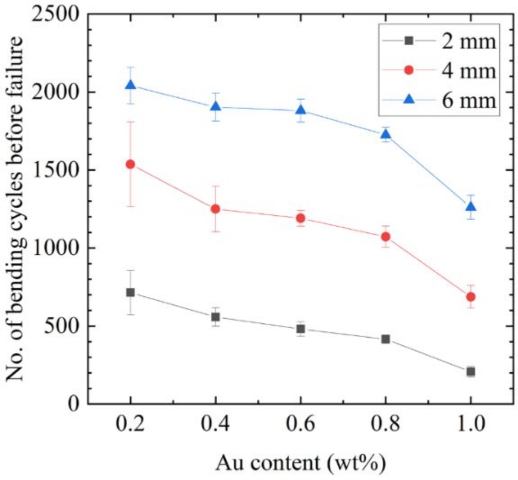

Fig. 7. Number of bending cycles before failure of the Au-PS hybrid films as a function of the bending radius.

chains after co-dispersion. The high-magnification TEM image in Fig. 3 shows the NP size and distribution, which again confirms that the NPs are less than 5 nm and have a narrow size distribution.

Fig. 4 shows the XRD patterns of the synthesized Au nanoparticles. The well-defined diffraction peaks are consistent with previously reported peaks of face centre cubic Au crystal structure.[65]

The transparency of the hybrid films with an Au NP concentration from 0 to 1 wt% is shown in Fig. 5. The pure PS film is totally transparent. Since the Au NPs have a dark, almost black color, the color of the hybrid films becomes darker with the Au NP concentration increase, which leads to a decrease in the film transparency. This result follows transmittance curves of each film obtained from the UV-Vis tests (Fig. S1 in the Supplementary information). The films with lower Au NP contents show higher transmittance at the visible light range. This means that the higher contents are more effective in photon trapping and plasmonic coupling, consequently leading to an increase in the visible light absorption.

The interparticle distance can provide further understanding of the Au NP distribution in the Au-PS hybrid films. If we assume that the Au NPs are homogeneously distributed in the PS matrix, the ideally appropriated volume space, V_{free}, for a specific Au NP and its surrounding PS matrix can be calculated as:[66]

$$(V_{Au-PS} - V_{PS})/V_{Au} = n \qquad (6)$$

$$V_{Au-PS}/n = V_{free} \qquad (7)$$

where V_{Au-PS} is the volume of a collection of Au NPs and the surrounding PS matrix under an idealized distribution condition, V_{PS} the volume of the PS domain that can be assigned to a population of Au particles n, and V_{Au} the volume of one Au NP, respectively. With Eqs. (6 and 7), the Au NP surface-to-surface distance d can be determined by assuming a cubic lattice model for the Au NPs:[66]

$$d = L - 2r = V_{free}^{\frac{1}{3}} - 2r \qquad (8)$$

where r and L denote the radius of the Au NPs and the edge length of the cubic lattice, respectively. The calculated interparticle distances are shown in Fig. 6. The distance decreases in the order of 80.8, 63.1, 54.5, 49.1, and 45.2 nm as the Au NP concentration increases from 0.2 to 1 wt%. The interparticle distance decreases by ~44% when the concentration changes from 0.2 to 1 wt%. Considering the small Au NP size (<5 nm), the particles would still have ample space to stay separated.

Fig. 7 shows the numbers of cycles before the Au-PS films fail at different bending radii. With an increase in the bending radius from 2 to 6 mm, the number of cycles also increases. For example, the number of cycles for the 0.2 wt% Au-PS sample changes from 715 to 2041 when the bending radius increases from 2 to 6 mm. As the Au content increases, the number of cycles steadily decreases. At the highest Au content of 1.0 wt%, the number of bending cycles before failure increases from 207 to 1261 when the bending radius increases from 2 to 6 mm. The results mean that these hybrid films are very flexible and can sustain repeated use. Even though the number of cycles decreases with the Au NP concentration, in general a larger bending radius leads to a higher number of cycles before failure. The number of cycles decreases only slightly with the Au content up to 0.8 wt% but more significantly at 1.0 wt%.

Photothermal healing

An increase in the Au NP concentration means an increase in the number of heat sources by the photothermal effect, which can result in high efficiency in the damage- and defect-healing of the hybrid films. For instance, when the laser with an intensity of 300 W/cm^2 was irradiated on a film having an acrylic resin matrix and 0.04 wt% Au NPs, the temperature of the film owing to the photothermal effect was 247 ℃, while the temperature was 76 ℃ for the film with 0.005 wt% Au NPs.[25]

For the Au-PS films in this work, without the Au NPs, no healing is observed regardless of the laser irradiation power or time (Fig. S2 in the Supplementary information), which demonstrates that the photothermal effect is caused by the plasmonic resonance of the Au NPs. Figs. 8 and 9 show the surface morphology of the continuously healed films with 0.2 and 1.0 wt% Au NPs, respectively, for 80 μm-sized indents as the laser healing time increases from 0 to 15 s. For the healing of the Au-PS hybrid films, the laser power has to be varied with the Au concentration for the healing to occur. The power used for the film with 0.2 wt% Au NPs (12.25 mW) is about 2.9 times larger than that used for the film with 1.0 wt% Au NPs (4.25 mW). Again, this demonstrates the photothermal effect from the Au NPs. With more Au NPs in the Au-PS hybrids, more photothermal heating is induced, which enables the healing of the PS film with less laser power. At both Au concentrations, the indent size gradually decreases from its edges to the center owing to the flow of the melting PS. From the DSC analysis, the glass transition temperatures of the hybrid films were observed at 97~99 °C, which is about 5 °C lower than that of the pure PS film (103 °C), similar to the previously reported trend.[67] This means that the healing process occurs above their glass transition temperatures. The indents are almost completely healed after 15 seconds of laser irradiation. The measured and extrapolated temperatures of the films during irradiation are presented in Fig. S3. The temperature range is from 190 to 304 °C with increasing Au NP content, which is higher than the glass transition temperature of PS.

Fig. 10 shows the amount of energy required to heal the indents of different sizes (30, 55, and 80 μm) in the hybrid films. As the indent size increases, the healing energy required to close the indent also increases. The increased energy is attributed to the increasing depth of the indent, since the energy transmitted to the film decreases as the laser size increases, which depends on the distance between the laser source and the target. From a different perspective, the energy decreases with the Au NP concentration up to 0.6 wt% Au NPs, which reflects the increased efficiency of the healing process owing to the increasing number of heat sources from the Au NPs and thus more significant plasmonic coupling effect. For example, the energy needed to heal the 80 μm indent is 159.3

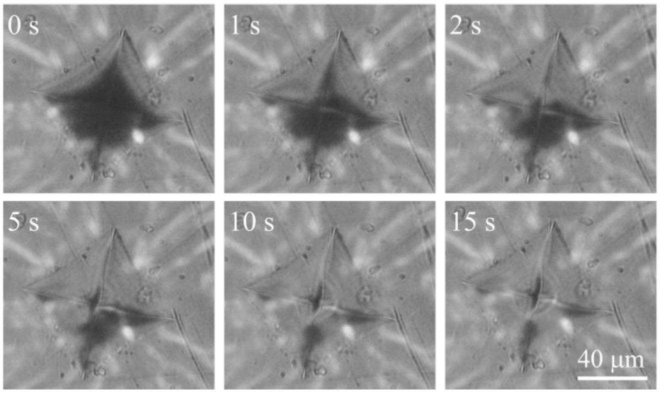

Fig. 8. Morphological evolution for an 80 μm-sized indent in the hybrid film with 0.2 wt% Au NPs.

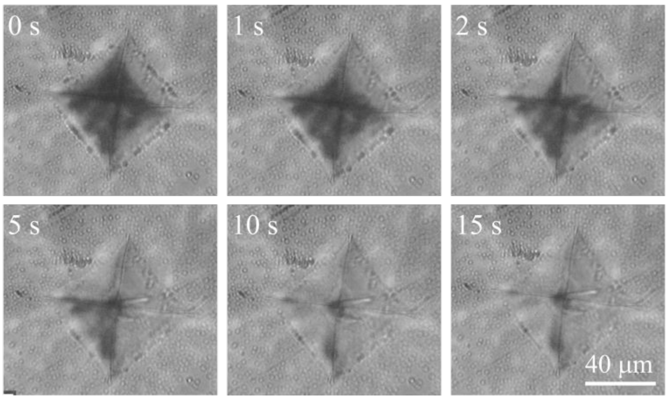

Fig. 9. Morphological evolution for an 80 μm-sized indent in the hybrid film with 1.0 wt% Au NPs.

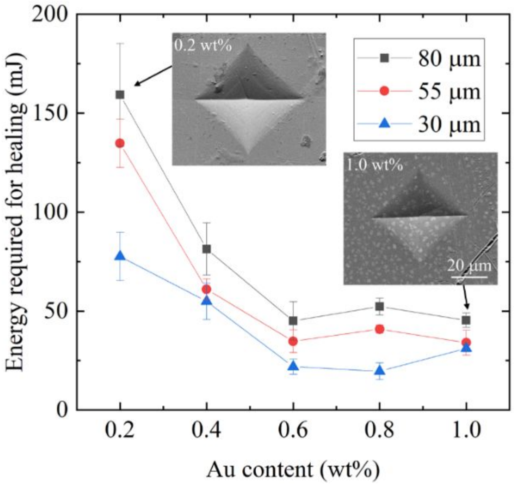

Fig. 10. Laser energy required to heal different size indents vs. the Au content in the Au-PS hybrids. The inserts are the indent SEM images at different Au contents.

mJ for the films with 0.2 wt% Au NPs, while only 45.3 mJ for the hybrid film with 1.0 wt% Au NPs.

Fig. 10 also shows that the Au content plays a more significant role than the indent size in required energy for healing at low Au content levels (≤0.6 wt%). The required energy to heal the same indent size, however, remains almost the same when the Au NP content is ≥ 0.6 wt%. This behavior is new and contrary to the general notion that more Au NPs should lead to a higher photothermal heating effect. One reason is that since the concentration of the Au NPs is relatively high compared to the previous study (0.04 wt%),[25] agglomeration of the Au NPs takes place in the film. The inhomogeneous distribution of the NPs may deteriorate the photothermal properties, which is directly related to the interparticle distance between the NPs. This agglomeration phenomenon can be seen as shown in the inserts of Fig. 10 for 0.2 wt% and 1.0 wt% Au-PS hybrids. At 0.2 wt% Au concentration, no agglomeration of Au NPs is observed. However, at 1 wt% Au content, Au NP agglomeration can be easily observed by the lighter color domains. The impact of the Au NP agglomeration on the photothermal effect and thus healing ability is also further demonstrated through the simulation results below.

Photothermal simulation

The finite element simulations conducted include efforts to study the effects of the volume fraction and particle agglomeration on the temperature rise induced by the photothermal effect. Fig. 11 shows the maximum temperature of the hybrid films with randomly distributed Au NPs after the laser irradiation. Also, the estimated temperatures obtained from the experiments (Fig. S3) are plotted for comparison. The estimated temperatures are higher than those from the simulation except for the 0.8 wt% Au NP film because of the linear fitting assumption made during the temperature extrapolation. The trend difference from the 0.8 to 1.0 wt% Au NP films is attributed to a lack of consideration of the agglomeration effect during the temperature extrapolation. The laser intensity used for each analysis is also plotted, which is kept the same as that used in the healing tests. The maximum temperature slightly decreases from 164 to 151 °C for the films with 0.2 to 0.6 wt% Au NPs, even with the large decrease in the laser intensity. This result corresponds well to that from the healing tests in Fig. 10. Although the laser intensity decreases with an increase in the concentration of the Au NPs, the healing still occurs. This is because a lower energy is required due to the large number of heat sources (increasing Au NP population). For the higher concentrations (≥0.8 wt%), the simulation results show that the healing temperatures are above 260 °C. We believe that this temperature is higher than the actual temperature in the Au-PS hybrid film because the models here represent idealized phase dispersion in the Au NP-PS hybrids. This means that the hybrid films with 0.8 and 1.0 wt% Au NPs are assumed to possess a highly homogeneous microstructure with no agglomeration of the NPs. In the actual samples, Au NP agglomeration has been observed as shown in the insert of Fig. 10. Regarding the large temperature difference between the samples at ≤0.6 wt% Au content and at ≥0.8 wt% Au content, the films with 0.8 and 1.0 wt% Au NPs could be affected by the localized spatial distribution of the NPs. Concentrated Au NPs can cause local over-heating under the laser irradiation even though the temperature across the large scale of the Au-PS film

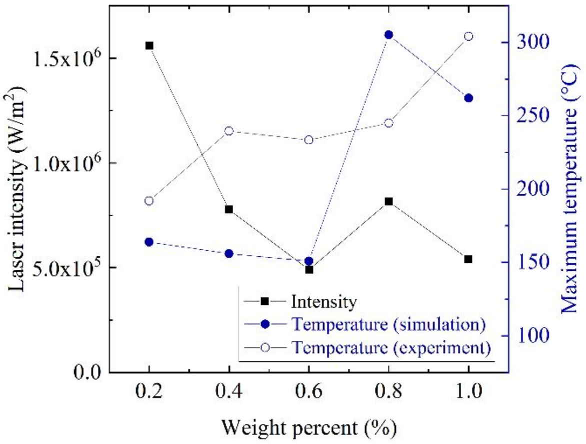

Fig. 11. Laser intensity applied during the healing process and simulated temperature in the hybrid films as a function of the Au NP concentration with the experimental temperature for comparison.

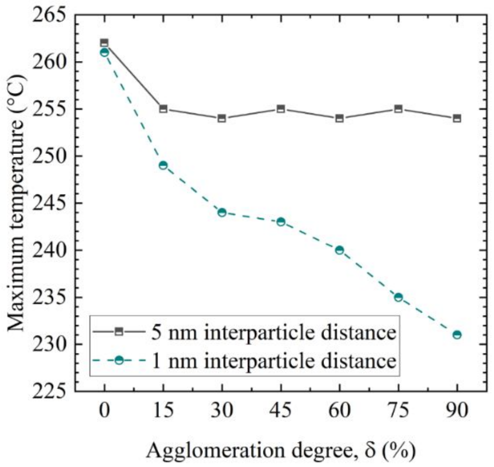

Fig. 12. Agglomeration effect of the Au NPs on the maximum temperature in the hybrid films.

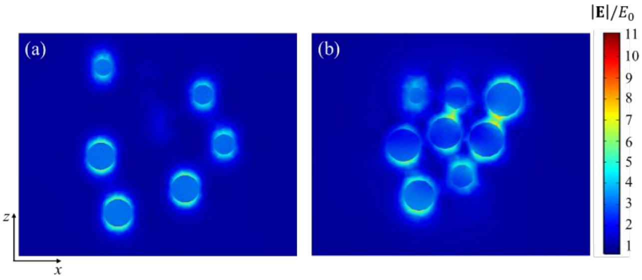

Fig. 13. Cross-sections of the electric field ($|\mathbf{E}|/E_0$) and the corresponding photothermal enhancement of the agglomerated regions of the Au NPs with (a) 5 and (b) 1 nm interparticle distances. The incident beam travels along the x-axis and polarized along the z-axis.

is actually low. Comparing with the experimental results, the laser intensity for the photothermal healing should decrease with the Au concentration increase from a theoretical point of view. However, the actual Au-PS films with 0.8 and 1.0 wt% Au NPs require a higher intensity than the lower Au content films for the indent healing. This also supports the agglomeration effect on the local photothermal behaviors.

Fig. 12 shows the effect of the Au NP agglomeration on the maximum temperature of the hybrid films. Two different interparticle distances of 5 and 1 nm are set in the agglomeration models. For the agglomeration models with 5 nm interparticle distance, the maximum temperature decreases from 262 to 254 °C, shown as black square markers in Fig. 12. The agglomeration of the NPs reduces the photothermal effect even though the magnitude is insignificant. On the other hand, the films with the agglomerated Au NPs at 1 nm interparticle distance show a different behavior (the line with circle markers). The temperature in the hybrids decreases with the Au NP concentration from 261 to 231 °C. This is because the plasmonic coupling depends on the distance between the NPs.[68] Especially, if the distance becomes shorter than the particle size, the coupling is more significant.[69] Since the main difference between the two models is the interparticle distance, the coupling in-between the Au NPs (the actual particle-particle separation distance) significantly influences the photothermal effect.

The electric field enhancement effect of the Au-PS hybrid films with 5 and 1 nm interparticle distances is shown in Fig. 13. No strong plasmonic coupling is observed for the 5 nm interparticle distance condition (Fig. 13(a)). Small enhancement is located at the top and the bottom of the NPs. This distribution is the same as the one from the models without the Au NP agglomeration. On the other hand, strong plasmonic coupling is found near the NPs, especially along the polarization axis (z). For the 1 nm interparticle distance condition, the plasmonic coupling is significantly enhanced as shown in Fig. 13(b). The maximum plasmonic enhancement of the film with 1 nm Au interparticle distance is 1.56 times larger than that with the 5 nm interparticle distance. This large difference can be understood from the laser absorption cross-section difference. Since the photothermal heating effect is a function of the absorption cross-section, laser intensity, and volume of single Au NPs, when the latter two factors are kept the same, the agglomeration affects the absorption cross-section of the NPs. The average absorption cross-sections of the films with 5 and 1 nm interparticle distances are calculated as 11.2 and 10.1 nm^2, respectively. This difference demonstrates the changes in the amount of heat energy generated in the hybrid films during the laser irradiation. As a result, the agglomeration of the Au NPs lowers the efficiency of the photothermal healing.

Conclusions

In this study, the synthesis and photothermal healing properties of the Au-PS hybrid films are investigated. The hybrid films with the Au NP concentration up to 1 wt% are successfully fabricated. The Au NP distribution in the hybrids is a strong function of the Au NP concentration. The hybrid films show great flexibility and transparency, which decrease with the Au NP concentration. Laser irradiation can successfully heal different size indents created in the hybrid films, as a function of the Au NP contents and indent sizes. The simulation results have good agreement with the experimental results and demonstrate that the photo-induced heating is influenced by the NP agglomeration and interparticle distance along with plasmonic coupling. Because of the agglomeration, a proper selection of the Au NP concentration will lead to high self-healing efficiency, high flexibility, and high transparency with less agglomeration, eventually a more viable hybrid film. The developed hybrid films can be utilized for functional electric components requiring high flexibility and no contact healing.

Conflicts of interest

There are no conflicts to declare.

Acknowledgements

We acknowledge the financial support from National Science Foundation under grant number CMMI-1661564.

References

1 T. Hanemann and D. V. Szabó, *Materials*, 2010, **3**, 3468-3517.
2 T. Tanaka, G. C. Montanari and R. Mulhaupt, *Ieee T Dielect El In*, 2004, **11**, 763-784.
3 Q. Wang and L. Zhu, *J Polym Sci Pol Phys*, 2011, **49**, 1421-1429.
4 Z.-M. Dang, J.-K. Yuan, J.-W. Zha, T. Zhou, S.-T. Li and G.-H. Hu, *Prog Mater Sci*, 2012, **57**, 660-723.
5 P. Köberle and A. Laschewsky, *Macromol Symp*, 1994, **88**, 165-175.
6 H. H. Althues, J; Kaskel, S, *Chem Soc Rev*, 2007, **36**, 1454-1465.
7 K. S. M. Narayan, A G; Nanda, J; Sarma, D D, *Appl Phys Lett*, 1999, **74**, 871-873.
8 Y. Tu, L. Zhou, Y. Z. Jin, C. Gao, Z. Z. Ye, Y. F. Yang and Q. L. Wang, *J Mater Chem*, 2010, **20**, 1594.
9 Y. F. Lin, K. Lu and R. Davis, *Langmuir*, 2019, **35**, 5855-5863.
10 M. Gervasio and K. Lu, *J Phys Chem C*, 2017, **121**, 11862-11871.
11 H. W. Cao, P. Yang and B. Z. Bao, *Adv Mat Res*, 2011, **383-390**, 483-489.
12 C. Kim and C. H. Kim, *Micromachines*, 2018, **9**, 492-504.
13 T. W. Kim, J. S. Lee, Y. C. Kim, Y. C. Joo and B. J. Kim, *Materials*, 2019, **12**, 2490-2498.
14 S.-M. Yi, I.-S. Choi, B.-J. Kim and Y.-C. Joo, *Electron Mater Lett*, 2018, **14**, 387-404.
15 Y. Yang, M. H. Yang, S. M. Zhang, X. Lin, Z. M. Dang and D. R. Wang, *J Appl Polym*, 2019, **136**, 47158-47167.
16 J. Ko, Y. J. Kim and Y. S. Kim, *Acs Appl Mater Inter*, 2016, **8**, 23854-23861.
17 Y. J. Tan, J. K. Wu, H. Y. Li and B. C. K. Tee, *Acs Appl Mater Inter*, 2018, **10**, 15331-15345.
18 D. Y. Wu, S. Meure and D. Solomon, *Prog Polym Sci*, 2008, **33**, 479-522.
19 N. J. Kanu, E. Gupta, U. K. Vates and G. K. Singh, *Compos Part A Appl Sci Manuf*, 2019, **121**, 474-486.
20 Y. Yang and M. W. Urban, *Chem Soc Rev*, 2013, **42**, 7446-7467.
21 S. A. Haddadi, A. Ramazani S.A, M. Mahdavian, P. Taheri, J. M.

C. Mol and Y. Gonzalez-Garcia, *Compos B Eng*, 2019, **175**, 107087.
22 M. W. Lee, S. An, S. S. Yoon and A. L. Yarin, *Adv Colloid Interface Sci*, 2018, **252**, 21-37.
23 B. Zhang, W. Zhang, Z. Zhang, Y.-F. Zhang, H. Hingorani, Z. Liu, J. Liu and Q. Ge, *Acs Appl Mater Inter*, 2019, **11**, 10328-10336.
24 Y. Yang, J. He, Q. Li, L. Gao, J. Hu, R. Zeng, J. Qin, S. X. Wang and Q. Wang, *Nat Nanotechnol*, 2019, **14**, 151-155.
25 P. Peng, B. Zhang, Z. Cao, L. Hao, F. Yang, W. Jiao, W. Liu and R. Wang, *Compos Sci Technol*, 2016, **133**, 165-172.
26 Z. Cao, R. Wang, F. Yang, L. Hao, W. Jiao, W. Liu, Q. Wang and B. Zhang, *RSC Adv*, 2015, **5**, 102167-102172.
27 L. Chen, L. P. Si, F. Wu, S. Y. Chan, P. Y. Yu and B. Fei, *J Mater Chem C*, 2016, **4**, 10018-10025.
28 V. Amendola, R. Pilot, M. Frasconi, O. M. Marago and M. A. Iati, *J Phys Condens Matter*, 2017, **29**, 203002.
29 H. J. Chen, L. Shao, Q. Li and J. F. Wang, *Chem Soc Rev*, 2013, **42**, 2679-2724.
30 X. C. Ye, C. Zheng, J. Chen, Y. Z. Gao and C. B. Murray, *Nano Lett*, 2013, **13**, 765-771.
31 C. H. Fang, G. L. Zhao, Y. L. Xiao, J. Zhao, Z. J. Zhang and B. Y. Geng, *Sci Rep*, 2016, **6**, 1-8.
32 N. Jiang, X. Zhuo and J. Wang, *Chem Rev*, 2018, **118**, 3054-3099.
33 A. J. Haes, C. L. Haynes, A. D. McFarland, G. C. Schatz, R. P. Van Duyne and S. Zou, *MRS Bull*, 2005, **30**, 368-375.
34 Y. Xia and N. J. Halas, *MRS Bull*, 2005, **30**, 338-348.
35 K. Setoura, D. Werner and S. Hashimoto, *J Phys Chem C*, 2012, **116**, 15458-15466.
36 H. Petrova, J. P. Juste, I. Pastoriza-Santos, G. V. Hartland, L. M. Liz-Marzan and P. Mulvaney, *Phys Chem Chem Phys*, 2006, **8**, 814-821.
37 S. Link and M. A. El-Sayed, *Int Rev Phys Chem*, 2000, **19**, 409-453.
38 J. Brandrup, E. H. Immergut, E. A. Grulke, A. Abe and D. R. Bloch, *Polymer handbook*, Wiley New York, 1999.
39 J. Shin, M. Song, H. Hafeez, P. J. Jeusraj, D. H. Kim, J. C. Lee, W. H. Lee, D. K. Choi, C. H. Kim, T.-S. Bae, S. M. Yu, K.-H. Kim, H.-G. Park, K.-B. Chung, A. Song, Y.-C. Kang, J. Park, C. S. Kim and S. Y. Ryu, *Org Electron*, 2019, **66**, 94-101.
40 S. Hashimoto, D. Werner and T. Uwada, *J Photoch Photobio C*, 2012, **13**, 28-54.
41 Q. Su, S. King, L. Y. Li, T. Y. Wang, J. Gigax, L. Shao, W. A. Lanford and M. Nastasi, *Scripta Mater*, 2018, **146**, 316-320.
42 N. J. Halas, S. Lal, S. Link, W. S. Chang, D. Natelson, J. H. Hafner and P. Nordlander, *Adv Mater*, 2012, **24**, 4842-4877.
43 A. O. Govorov and H. H. Richardson, *Nano Today*, 2007, **2**, 30-38.
44 P. K. Jain, W. Y. Huang and M. A. El-Sayed, *Nano Lett*, 2007, **7**, 2080-2088.
45 T. Atay, J. H. Song and A. V. Nurmikko, *Nano Lett*, 2004, **4**, 1627-1631.
46 A. M. Funston, C. Novo, T. J. Davis and P. Mulvaney, *Nano Lett*, 2009, **9**, 1651-1658.
47 J. A. Scholl, A. Garcia-Etxarri, A. L. Koh and J. A. Dionne, *Nano Lett*, 2013, **13**, 564-569.
48 S. K. Ghosh and T. Pal, *Chem Rev*, 2007, **107**, 4797-4862.
49 E. Messina, E. Cavallaro, A. Cacciola, M. A. Iati, P. G. Gucciardi, F. Borghese, P. Denti, R. Saija, G. Compagnini, M. Meneghetti, V. Amendola and O. M. Marago, *Acs Nano*, 2011, **5**, 905-913.
50 B. Luk'yanchuk, N. I. Zheludev, S. A. Maier, N. J. Halas, P. Nordlander, H. Giessen and C. T. Chong, *Nat Mater*, 2010, **9**, 707-715.
51 X. Chen, A. Munjiza, K. Zhang and D. Wen, *J Phys Chem C*, 2014, **118**, 1285-1293.
52 S.-i. Yanagiya, N. Sekimoto and A. Furube, *Jpn J Appl Phys*, 2018, **57**, 115001.
53 T. Grosges and D. Barchiesi, *Molecules*, 2018, **23**, 1316-1328.
54 I. Aibara, S. Mukai and S. Hashimoto, *J Phys Chem C*, 2016, **120**, 17745-17752.
55 K. Setoura, Y. Okada, D. Werner and S. Hashimoto, *Acs Nano*, 2013, **7**, 7874-7885.
56 M. Enders, S. Mukai, T. Uwada and S. Hashimoto, *J Phys Chem C*, 2016, **120**, 6723-6732.
57 Y. R. Davletshin and J. C. Kumaradas, *Beilstein J Nanotechnol*, 2016, **7**, 869-880.
58 Z. C. Zeng, H. Wang, P. Johns, G. V. Hartland and Z. D. Schultz, *J Phys Chem C*, 2017, **121**, 11623-11631.
59 G. Palermo, U. Cataldi, A. Condello, R. Caputo, T. Burgi, C. Umeton and A. De Luca, *Nanoscale*, 2018, **10**, 16556-16561.
60 B. Chen and K. Lu, *Langmuir*, 2011, **27**, 4117-4125.
61 P. K. Jain and M. A. El-Sayed, *Chem Phys Lett*, 2010, **487**, 153-164.
62 J.-M. Jin, *The finite element method in electromagnetics*, John Wiley & Sons, New Jersey, 2015.
63 D. F. Santos, A. Guerreiro and J. M. Baptista, *Photonic Sensors*, 2013, **3**, 61-66.
64 B. Widom, *J Chem Phys*, 1966, **44**, 3888-3894.
65 S. Krishnamurthy, A. Esterle, N. C. Sharma and S. V. Sahi, *Nanoscale Res. Lett.*, 2014, **9**, 627.
66 C. P. Li, C. H. Wu, K. H. Wei, J. T. Sheu, J. Y. Huang, U. S. Jeng and K. S. Liang, *Adv Funct Mater*, 2007, **17**, 2283-2290.
67 H. Oh and P. F. Green, *Nat Mater*, 2009, **8**, 139-143.
68 G. Bachelier, I. Russier-Antoine, E. Benichou, C. Jonin, N. Del Fatti, F. Vallée and P. F. Brevet, *Phys Rev Lett*, 2008, **101**, 197401.
69 U. Kreibig and L. Genzel, *Surf Sci*, 1985, **156**, 678-700.

Table of Contents Entry

TITLE: Photothermal self-healing of gold nanoparticle-polystyrene hybrids

Yi Je Cho, Lingchen Kong, Rezawana Islam, Meitong Nie, Wei Zhou, and Kathy Lu

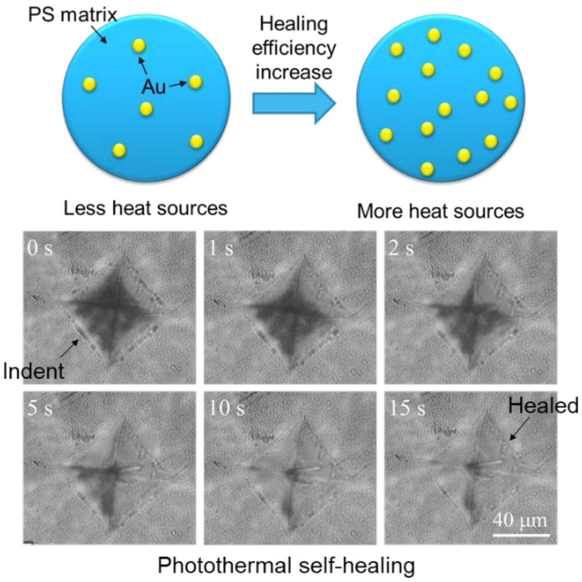

Photothermal self-healing efficiency increased with Au nanoparticle contents and particle agglomeration deteriorated the efficiency.